Solid Earth forcing of Mesozoic oceanic anoxic events

T. M. Gernon[a], B. J.W. Mills[b], T. K. Hincks[a], A. S. Merdith[b,c], L. J. Alcott[d,e,f,g], E. J. Rohling[a,h], M. R. Palmer[a]

[a] *School of Ocean & Earth Science, University of Southampton, Southampton SO14 3ZH, UK*
[b] *School of Earth & Environment, University of Leeds, Leeds LS2 9TJ, UK*
[c] *School of Physics, Chemistry and Earth Sciences, University of Adelaide, Adelaide, Australia*
[d] *Department of Earth & Planetary Sciences, Yale University, New Haven, CT, USA*
[e] *Yale Institute for Biospheric Studies, Yale University, New Haven, CT, USA*
[f] *Department of Earth & Environmental Sciences, University of Waterloo, Waterloo, Ontario, Canada*
[g] *Now at: School of Earth Sciences, University of Bristol, Bristol BS8 1RJ, UK*
[h] *Department of Earth Sciences, Utrecht University, Princetonlaan 8a, 3584 CB Utrecht, Netherlands*

Oceanic anoxic events are geologically abrupt phases of extreme oxygen depletion in the oceans that disrupted marine ecosystems and brought about evolutionary turnover. Typically lasting ∼1.5 million years, these events occurred frequently during the Mesozoic era, from about 183 to 85 million years ago, an interval associated with continental breakup and widespread large igneous province volcanism. One hypothesis suggests that anoxic events resulted from enhanced chemical weathering of Earth's surface in a greenhouse world shaped by high volcanic carbon outgassing. Here, we test this hypothesis using a combination of plate reconstructions, tectonic-geochemical analysis, and global biogeochemical modelling. We show that enhanced weathering of mafic lithologies during continental breakup and nascent seafloor spreading can plausibly drive a succession of anoxic events. Weathering pulses collectively gave rise to substantial releases of the nutrient phosphorus to the oceans, stimulating biological primary production. This, in turn, enhanced organic carbon burial and caused widespread ocean deoxygenation on a scale sufficient to drive recurrent anoxia. This model complements volcanic outgassing-centred hypotheses for triggering these events by demonstrating well-quantified basaltic sources of phosphorus release during periods of intense weathering related to climate warmth. Our study highlights a close coupling between the solid Earth and biosphere during continental reorganisation.

Oceanic anoxic events (OAEs) are transient perturbations to the global carbon cycle, during which large regions of the oceans are depleted in dissolved oxygen[1,2]. The resulting euxinic (i.e., anoxic and sulfidic) waters are highly toxic, leading to biological turnover events, and in extreme cases, mass extinctions of marine biota[2]. For example, the Toarcian OAE involved a ∼70%

Preprint submitted to Nature Geoscience *May 17, 2024*

reduction in the diversity of some benthic fauna[3]. It is widely accepted that OAEs are ultimately linked to global warming[2], which intensifies the hydrological cycle[4] and chemical weathering on the continents[5,6]. These conditions lead to increased primary production and organic matter burial in the oceans[7], documented in the geological record as organic-rich black shales[1] (Fig. 1). These processes, in turn, cause a significant reduction in deep-water O_2 concentration ($[O_2]$).

Other Phanerozoic OAEs include the Steptoean Positive Carbon Isotope Excursion (SPICE), the Hirnantian OAE (HOAE), the Frasnian-Famennian (F–F) and the Permian-Triassic boundary event (P–T)[4]. However, the Mesozoic brought multiple OAEs in close succession (Figs. 1–2), with a mean duration of 1.4 million years (Myrs) and a recurrence interval of ~7 Myrs (Extended Data Table 1). Earth system models implicate a role for continental configuration in promoting deoxygenation of Mesozoic ocean shelves[8]. However, the interconnected nature of coeval environmental processes, including carbon outgassing from volcanogenic and/or methanogenic sources, global warming, increases in thermohaline circulation, and changes in nutrient cycling, leaves the first-order drivers of OAEs open to debate.

OAEs and Large Igneous Provinces

OAE initiation has been attributed to intensified carbon dioxide (CO_2) emissions from Large Igneous Provinces (LIPs)[9,10] (Fig. 1), many of which coincide with known anoxic events (Fig. 2b). Uncertainties in LIP ages, typically ±1 Myrs (similar to mean OAE duration), and intervals of activity up to 40 Myrs (Fig. 2b)[11], pose challenges for establishing conclusive linkages. A compounding factor is that LIPs are typically associated with continental rifted margins where other geological processes co-occur[12]. There is no doubt, however, that the high frequency of LIPs (Fig. 2b) contributed to the prolonged greenhouse conditions of the late Mesozoic that promoted intense chemical weathering. The question is whether LIP emplacement initiates an instantaneous weathering response. Global chemical weathering intensity over the past 400 Myrs is only weakly correlated with both the total eruptive area, and LIP area within the tropics[6], implicating other factors. However, the influence of LIPs peaks 35–50 Myrs after emplacement[6], perhaps indicating a delayed weathering response associated with passive margin rejuvenation[13].

The Mesozoic era brought substantial changes in global ocean chemistry, including several carbon isotope excursions (Figs. 2c–f). These changes do not provide an unambiguous record of the relative magnitude of weathering inputs, as geochemical proxies record contributions from multiple, simultaneous geological processes[6]. For example, the gradual increase in seawater $^{87}Sr/^{86}Sr$ (Fig. 2f) reflects increased weathering related to arc volcanism and continental breakup[6] (Fig. 2h). Further, the long oceanic residence time of Sr (~5 Myr) limits its utility in identifying OAE drivers. While $^{187}Os/^{188}Os_{initial}$ (Os_i) signatures offer more promise, a substantial osmium input from continental weathering sources could plausibly mask a volcanic signal (and vice versa), even if volcanism was the first-order driver of global anoxia.

Global tectonic reorganisation of the Mesozoic

We propose that processes associated with continental breakup plausibly drove many Mesozoic OAEs (Fig. 2f). Breakup and mid-ocean ridge assembly reached peak intensity during the major interval of OAEs (Figs. 2a, 2g, 2h). The 'rift-to-drift' transition and associated uplift of continental margins generates extensive volcanic terrains, which, in turn, leads to increased weathering of mafic lithologies. Volcanic rocks such as basalts are enriched in phosphorus (P)[14,15], a biolimiting nutrient that regulates burial of organic matter over geological timescales[16]. Enhanced weathering of such rocks supplies nutrients to oceans, influencing bioproductivity[17,18]. For instance, excess delivery of bioavailable P can lead to eutrophic conditions that deplete water column [O_2], causing widespread anoxia or euxinia[19]. Such conditions can be sustained over million-year timescales via further recycling of P from sediments overlain by anoxic or euxinic waters, as indicated by observations[20,21] and models[19,22] of the Cenomanian-Turonian OAE (OAE 2). Like the weathering of mafic rocks on land[15], volcanism during mid-ocean ridge formation contributes essential nutrients, including P, directly to the global ocean through submarine weathering[14].

Incipient mid-ocean ridges

During the Mesozoic, the breakup of Gondwana (Fig. 2f–g) involved a protracted, ~120-

Myr-long episode of mid-ocean ridge assembly on a global scale (Figs. 1, 2a, 3). In addition to fragmenting the continents and increasing global weatherability[6], this process generated narrow ocean basins (Figs. 1, 3a; Extended Data Fig. 1) where restricted water circulation can cause limited ventilation of bottom waters, locally encouraging the expansion of anoxia and euxinia. Although enhanced weathering can increase organic carbon burial, removing atmospheric CO_2 and causing global cooling, this process may be counteracted by the expansion of the global ridge system — increasing net carbon outgassing into the oceanic reservoir[23], contributing to increased dissolved inorganic carbon (DIC) and driving ocean CO_2 degassing on geologically short timescales[24].

Extensional plate boundaries are a key source of nutrients to the oceans during breakup[14]. When continental rift basins submerge below sea level, it results in extensive volcanic-seawater interactions and accelerated chemical weathering of volcanic regolith. In such transitional environments, referred to here as incipient mid-ocean ridges (MORs), enhanced volcanism driven by magma-seawater interactions, coupled with low hydrostatic pressures, also promotes the explosive eruption of basalt[25]. To explore the impact of MOR assembly on ocean chemistry, we first investigate the spatial extent of mature continental rifts that transitioned to nascent ridges within relatively shallow ocean basins, defined here as <1,500 m deep (Extended Data Fig. 1; Methods). We identify nine incipient ridge segments using the plate-tectonic reconstruction software, GPlates[26] (https://www.gplates.org/). We find ~26,000 km of MOR initiated during the Jurassic–Cretaceous, 85% of which was simultaneously active from 160–120 Ma (Fig. 3b–d). Analysing seafloor production rates along these ridges, we find that the main incipient MORs overlap in timing with the main OAE interval (Fig. 3d). In northern latitudes, this includes a prolonged phase of oceanic anoxia within the Kimmeridgian, which, whilst not strictly an OAE, is considered one of the most prominent organic carbon burial episodes of the Phanerozoic[27]. During OAE 2, $\delta^{13}C$ excursions—signalling changes in both local and global carbon cycles—are attributed to basalt-seawater interactions[20], consistent with coeval sharp declines in Os_i in marine sediments[28] (Fig. 2e). Here, expanded deoxygenation preceded massive organic carbon burial, reflecting dynamic changes in oceanic redox conditions[29].

Within incipient MOR environments, fragmental, glass-rich basalts undergo rapid alteration, releasing a substantial fraction of elements, including phosphorus, into seawater[14] (Extended Data Fig. 2). Further, incipient MORs coincide with the rift-to-drift phase when decompression melting and upwelling of asthenospheric melts tend to be highest[30] and are typically characterised by an order of magnitude increase in magmatic productivity[31]. This phase of seafloor volcanism can plausibly transform large domains of oceanic crust from minor sinks[32] into net sources[14] of phosphate (Figs. 2d–f). Hyaloclastite breccias and other pyroclastic rocks are commonly formed during the transition from continental rifting to seafloor spreading and have been linked to early explosive magma-water interactions during submergence of the spreading axis[25]. For example, during the formation of the Central Atlantic Ridge[33] (Fig. 3a)—which unzipped to create the Hispanic Corridor (Fig. 1a)—a massive wedge of fragmental basaltic rocks was emplaced along the Atlantic margins of North America. With a volume of $\sim 3 \times 10^6$ km^3, this feature is one of Earth's largest igneous provinces[30].

We use seafloor production data to estimate P release from basalts emplaced along global ridges (Fig. 3). We use modelled lengths and spreading rates for each ridge to calculate seafloor ridge productivity over time (Figs. 3b–c). We simulate a linear decay in fragmentation and phosphorus release during seafloor subsidence, accounting for reduced weathering intensity as the ridge progressively deepens (see Methods). This analysis indicates that P release (Fig. 3f; Extended Data Fig. 3) potentially exceeded 3×10^{10} mol yr^{-1}, equivalent to over 75 percent of the current total reactive P flux from rivers to the oceans ($\sim 3.9 \times 10^{10}$ mol yr^{-1})[34].

Subaerial basalt uplift and weathering

Subaerial basalt weathering can deliver a substantial flux of bioavailable P to the ocean[15], boosting primary production and organic carbon burial, and driving global cooling[35]. Box models of oceanic phosphorus, carbon and oxygen cycles have demonstrated that increased P delivery from continents is sufficient to drive OAEs[19]. Alongside our ridge-derived P flux, we propose an additional riverine supply from a well-established phase of tectonic uplift and exhumation across Mesozoic southern Africa[13], which caused rapid denudation of thick subaerial flood basalts[36,37,38]. Previous thermochronological studies reveal multiple phases of abrupt cooling of rocks that correspond to erosion of approximately 2-km-thick basalts of Karoo-age (∼183 Ma)[36,37,39] (Methods; Figs. 4a–c), long (>30 Myr) after their eruption. A comparison between denudation rates and offshore sediment accumulation[36] indicates that three times more material was eroded than deposited in offshore basins at this time[37]. This deficit has been attributed to intense chemical denudation[37], consistent with humid subtropical climates regionally at this time[40]. This interpretation is supported by two geological observations: (1) coeval deltas dominated by clays derived from weathering of mafic lithologies[37]; (2) widespread chemogenic carbonates in offshore basins, locally >500 m thick and covering ∼330,000 km^2, purportedly derived from Cretaceous basalt alteration[41].

We next estimate the phosphorus release from weathering related to tectonic uplift in southern Africa (Fig. 4b–c; Methods). Here, major exhumation occurred between 120 and 85 Ma, with peaks at about 120, 112, 104 and 95 Ma (Fig. 4c), and denudation rates up to 125 to 175 m Myr^{-1} have been reported[36]. At this time, basalts encompassed the wider Karoo Basin—as evidenced by thermochronological constraints[37,39], basalt fragments preserved in deeply eroded kimberlite pipes, and the present-day footprint of feeder intrusions (Methods). We develop a simple model using existing thermochronological 'best fit' models to drive denudation rates (Fig. 4c), sampling observed P_2O_5 concentrations from a global compilation of Karoo-aged basalts (GeoROC Database; Methods). Our models estimate that P fluxes from the chemical denudation of the basalts potentially reach 3×10^{10} mol yr^{-1} (Fig. 4d)—a similar magnitude to the present-day dissolved inorganic P input to the ocean[34]. Previous studies have shown that P accumulation rates rise and reach a peak coinciding with the onset of OAE 2[21]. Our model suggests this could be due at least in part to increased delivery of phosphate from continents, giving rise to increased primary productivity, organic carbon burial, and black shale formation[21].

While it is important to recognise the influence of other paleogeographic features, such as the Central Pangaean Mountains (Fig. 1a), on continental weathering, constructing a fully integrated Earth system model is beyond the scope of our study. Consequently, our estimated phosphorus fluxes for this comparatively well-documented phase of erosion (Fig. 4) should be regarded as conservative minimum estimates. Considering age uncertainties within terrestrial and marine records (typically ±1–2 Myr), we observe good overall correspondence between the timings of peak weathering events and OAE occurrences (Figs. 4c–d). This prompts the question of whether this relationship is coincidental or causal.

Biogeochemical model

To interrogate whether basalt weathering in submarine and subaerial environments could have driven anoxia, we test the influence of phosphorus release events on oceanic [O_2] and examine how their timings relate to OAEs in the geological record (Fig. 2). We incorporate both submarine (Fig. 3; Extended Data Figs. 3–4) and terrestrial (Fig. 4) basalt weathering fluxes (Supplementary Data S2–S3) into a global biogeochemical model of carbon-oxygen-phosphorus cycles developed by Slomp and Van Cappellen[42] and adapted by Alcott et al.[43] (Extended Data Fig. 5). The model divides the ocean into proximal and distal shelf zones, a surface open ocean, and a deep ocean interior, and explicitly represents primary production and remineralisation, as well as the decreasing retention of P in sediments under anoxic conditions[21]. The ridge flux of P is injected into the model's deep ocean box, while the riverine weathering flux is delivered into the proximal shelf zone box. Following Tsandev and Slomp[19], we amend global ocean circulation to account for the warmer, more stagnant ocean of the later Mesozoic. We reduce open ocean vertical mixing to 70% relative to present day, which falls within sensitivity estimates of previous studies[19]. All other background forcings follow the long-term Earth evolution scenario from Alcott et al.[43] (Methods).

Figure 5 shows model runs through the Jurassic and Cretaceous incorporating both ridge (Fig. 5a; Extended Data Fig. 6) and riverine (Fig. 5b) P fluxes. Each ridge initiation and basalt uplift/weathering event is considered independently (Methods; Fig. 5; Extended Data Fig. 7), because the biogeochemical model does not yet fully incorporate feedbacks for atmospheric oxygen, e.g., terrestrial biosphere and wildfires[44]. Because organic carbon removal means liberation of O_2, later events would be applied in a modified high-oxygen state, which is not consistent with the geological record of broadly stable atmospheric oxygen levels across the Jurassic and

Cretaceous[45]. When viewing the model output in these terms, calculated P fluxes and input rates are sufficient to trigger substantial ocean deoxygenation (Extended Data Fig. 7). For T-OAE, our model predicts a prolonged phase of anoxia (Fig. 5a) that conforms with global-scale deoxygenation indicated by marine redox proxies, extending well beyond this event[3,46]. MOR initiation, along with the climate-altering impacts of Karoo-Ferrar volcanism[3,46] (Fig. 2b), can jointly reconcile the long-term unradiogenic Os_i signal bracketing the T-OAE.

The overall correspondence between predicted deoxygenation events and OAEs (Extended Data Table 1) appears moderately good. Modelled drops in $[O_2]$ broadly coincide with nine out of 11 confirmed OAEs (Fig. 5). Notably, OAEs 1c and 1d do not overlap with either ridge or riverine deoxygenation, occurring approximately 2 Myr before the modelled peak related to riverine inputs (Fig. 5b). Further, OAE 1b occurs ~3 Myr before the modelled peak in deoxygenation. However, it is important to consider the age uncertainties in uplift/weathering events and OAE ages (typically ±1–2 Myr). OAE 2 coincides with an apparently smaller-scale weathering event (Fig. 5). At the Jurassic-Cretaceous boundary, we predict a relatively minor deoxygenation event linked to ridge volcanism, despite no known OAE in this interval (Fig. 5a). To quantify model performance, we apply a simple classifier derived from estimated $[O_2]$ minima to predict OAE occurrence. We identify the minimum value of $[O_2]$ over all individual ridge and weathering model runs (Extended Data Fig. 8) and normalise this to give a value on the interval [0,1], which can be used as a predictor of OAE occurrence (a binary outcome). Performance is measured using the Receiver Operating Characteristic (ROC) curve (Methods), where the area under the curve (AUC) of 0.705 (95% confidence intervals: 0.660–0.750) signifies a good but imperfect overall predictive value (Extended Data Fig. 8) for OAE timing, outperforming random chance (Fig. 5c).

One feature of the OAE geochemical record that is difficult to reconcile with any model for their origin is the presence of both negative and positive excursions in $\delta^{13}C_{carb}$ values[20] (Figs. 1c–d). In general, increased productivity and eutrophication is expected to yield a positive $\delta^{13}C_{carb}$ signature (e.g., OAE 2), as predicted by our model. Hence, the presence of negative $\delta^{13}C$ requires a source of isotopically light carbon. Individual volcanic events may also release light δ^{13}C if they trigger processes such as permafrost melting and/or thermal metamorphism of mudrocks or coal[48], but this does not negate the role of P release through volcanic weathering in stimulating productivity and causing anoxia/euxinia.

Extent of seafloor anoxia

Our results suggest that most OAEs could be explained by an interplay between enhanced weathering of mafic rocks in submarine and subaerial environments (Fig. 5). Model uncertainty indicates that deoxygenation events yield mean decreases of up to ~110 μmol kg^{-1} [O_2] averaged across the ocean interior, representing a ~30% decrease in average marine [O_2]. As marine [O_2] is difficult to infer for the deep past, most geological estimates of OAE intensity instead focus on the fraction of seafloor overlain by anoxic water. This is also uncertain but appears to be between 1–10% of the seafloor for most events[4]. A simple estimation considers that present day anthropogenic deoxygenation has reduced mean [O_2] by about 2%, leading to an 85% expansion of oxygen minimum zones[49]. Thus, a ~30% reduction in [O_2] is expected to increase seafloor anoxia from the present 0.3% of the ocean floor to about 4%, which is broadly consistent with the magnitude of OAEs in the geological record[4,46]. Modelled probability distributions (Figs. 5a–b) show that basalt weathering can drive much higher degrees of deoxygenation, and in turn, more severe seafloor anoxia (Extended Data Fig. 6).

The proposed weathering mechanisms do not necessarily contradict models for OAE triggering which invoke episodic massive volcanism. Our model quantifies a complimentary source of P that could theoretically drive organic carbon accumulation in marine basins and substantial deoxygenation. This does not preclude the involvement of additional disturbances in the global carbon cycle — rather, it may operate alongside them, if not directly driving OAEs, making oceans more susceptible to anoxia triggering.

To conclude, we hypothesise that continental breakup resulted in elevated background phosphorus levels during the main interval of Mesozoic OAEs (Figs. 2, 3), sufficiently potent to drive both prolonged and abrupt phases of deoxygenation (Fig. 5). Specifically, multiple pulses of continental basalt weathering linked to Gondwana breakup (Fig. 4) coincide closely in time and magnitude with OAEs (Fig. 5). Both processes plausibly combined to deliver pulsed fluxes of nutrients to the oceans, driving high rates of organic carbon burial and recurrent anoxic events. The Upper Cretaceous decline of this tectono-magmatic activity may help reconcile the frequency and intensity of OAEs in Mesozoic oceans. Our results thus support a mechanistic link between solid Earth processes and anoxic events that caused profound biological turnover episodes [1,2,3]. The proposed feedbacks between continental reorganisation, magmatism, and anoxia warrant further investigation, and carry implications for understanding the environmental consequences of other breakup events during Earth history.

Acknowledgements

T.M.G. gratefully acknowledges funding from the WoodNext Foundation, a component fund administered by the Greater Houston Community Foundation. B.J.W.M. and A.S.M. were supported by the Natural Environment Research Council (NERC) grant NE/X011208/1. A.S.M. was also supported by the Australian Research Council DECRA Fellowship DE230101642. L.J.A. was supported by the Hutchinson Environmental Fellowship Program from the Yale Institute for Biospheric Studies at Yale University. We are grateful to Hugh Jenkyns for helpful discussions, Hironao Matsumoto for advice on Os isotope data, and to **three anonymous reviewers** for critical and insightful comments that greatly improved the manuscript. We thank Tegan Francis for assistance with GIS mapping and Annabelle Carrington for help compiling carbon isotope records. We acknowledge the late Maarten de Wit for many stimulating conversations on the Great Karoo and the potential role of South African denudation in shaping Cretaceous climates. For the purpose of open access, the author has applied a CC BY public copyright licence to any Author Accepted Manuscript version arising from this submission.

Author contributions

T.G. conceived the idea and analysed and interpreted data. T.H. performed analysis of submarine and subaerial weathering, as well as the probabilistic analysis. B.J.M. led the global biogeochemical modelling component, with significant input from L.J.A. A.S.M. contributed data analysis in pyGPlates. E.J.R. and M.R.P. contributed expertise in chemical weathering and contributed to interpretation. T.G. drafted the manuscript and prepared the figures; all authors contributed to the writing and editing of the paper.

Competing interests

The authors declare no competing interests.

Corresponding author

Correspondence to Thomas Gernon (T.M.Gernon@soton.ac.uk).

Figure captions

Figure 1: Global distribution of oceanic anoxic event (OAE) sedimentary deposits and plate boundary features | Plate tectonic reconstructions from GPlates[26] (https://www.gplates.org/) (Methods) showing the main paleogeographic features, mid-ocean ridges, and exposed large igneous provinces, as well as the distribution of OAE-related sequences in the **a,** Toarcian OAE at about 183–182 Ma (with OAE sites from ref.[50] and references therein), and **b,** Turonian at about 90 Ma (with OAE sites from ref.[51] and references therein). Note that shallow seas include epicontinental seaways including the Western Interior Seaway of North America; HALIP is the High Arctic Large Igneous Province.

Figure 2: Tectonic, magmatic, and ocean chemical changes during the Mesozoic | a, Seafloor production rates (from ref.[6]) and total length of mid-ocean ridges and transform faults[52], and major phases of ocean basin formation (onset labelled): Afr–Antarc: Africa-Antarctica, Afr-Mad: Africa-Madagascar, and Aus-Mol: Australia Molucca; oceanic anoxic events (OAEs) are shown as horizontal beige bands (note that the Kimmeridgian* is not strictly an OAE and the dashed line for the Late-Hauterivian F-OAE is from ref.[53]); **b,** Large Igneous Provinces or LIPs (i.e., those with areas of $>200 \times 10^3$ km^2)[11]; also shown is the revised age range for the Ontong-Java Plateau[54]; **c,** $\delta^{13}C_{org}$ from organic-rich sediments[55], and, **d,** δ^{13}C from marine carbonates[56]; **e,** $^{187}Os/^{188}Os_i$ signatures of sediments (data sources provided in Extended Data Table 2); **f,** Seawater $^{87}Sr/^{86}Sr$ ratios from marine carbonates[57]; these ratios gradually increased during the Mesozoic in

step with Gondwana fragmentation (see **h**); **g,** Continental fragmentation index calculated using continental perimeter/area from plate reconstructions[58] (i.e., greater values signify higher degree of fragmentation, and vice versa); **h,** Simplified plate reconstructions showing Gondwana breakup (orthographic projection) based on the Ocean Drilling Stratigraphic Network magnetic reference frame (https://www.odsn.de/).

Figure 3: Scale of incipient mid-ocean ridges globally during the Mesozoic | a, Plate reconstructions for the Central Atlantic, Africa-Antarctica and South Atlantic incipient MOR systems, with synthetic isochrons showing the time (in Myr) relative to the reconstruction time (labelled; absolute ages in Ma are provided in brackets); see Extended Data Fig. 1 for all active Mesozoic ridge systems. **b,** Total ridge length, and **c,** mean full spreading rates for ridges based on ref.[59]; values shown in **b** and **c** are means for each ridge system over 30 Myr (Methods; Supplementary Data S1). **d,** Summary timeline of shallow ridge volcanism; oceanic anoxic events (OAEs) are shown as vertical grey bands, and the timing of precursory continental rifting[33] is depicted with horizontal bars. **e,** Summed magmatic productivity of shallow ridges from 200–60 Ma incorporating age uncertainty (see Methods), assuming water depths of <2 km for 30 Myr; inset shows longer-term context back to 350 Ma, where P-T is the Permo-Triassic anoxic event (linked to Siberian traps LIP) and PETM is the Palaeocene-Eocene Thermal Maximum (linked to North Atlantic LIP[31]), thought to represent an OAE[2]. **f,** Modelled combined ridge flux of P for all ridges active during this period (Extended Data Figs. 1 & 3), calculated in 10,000 simulations using ridge productivity data shown in **e**. Simulations account for uncertainty in the time of ridge initiation (see Methods).

Figure 4: Chemical denudation of continental basalts in the Mesozoic | a, Geological map of South Africa showing the distribution of Drakensberg basalts and their feeder intrusions (dark blue) within the Karoo Basin. **b,** Schematic cross section reconstructions at 120 and 110 Ma (line of section in **a**) based on apatite (U-Th)/He thermochronometry[39] and xenoliths in kimberlite pipes (modified after Stanley et al.[39]). **c,** Estimated cooling rate of rocks across South Africa from thermochronologic models[13] (see Methods) related to erosional exhumation between 160 and 80 Ma (hence age interval shown differs to Fig. 3), showing cooling trends associated with multiple regional events (Methods); the timing of oceanic anoxic events (OAEs*) are shown for context (*note the earliest event shown, the Kimmeridgian, is not strictly an OAE but involved prolonged phases of oceanic anoxia). **d,** Modelled annual flux of P from basalt denudation shown in **a**, utilising modelled cooling trends from thermochronology for individual localities across southern Africa to drive denudation rate (Methods).

Figure 5: Modelled ocean deoxygenation through time and observed timing of oceanic anoxic events (OAEs) | Mean, 5–95 percentile, and minimum–maximum estimates for dissolved [O_2] in the ocean interior over time from biogeochemical model simulations (see Methods for details). We input multiple (1,000) simulated phosphorus release events for **a,** shallow mid-ocean ridge systems, and **b,** riverine (continental weathering) sources tied to exhumation in southern Africa during and after Gondwana breakup (Fig. 4); OAEs are shown as vertical hatched bands (labelled); for both (**a**) and (**b**), upper plots show the P fluxes as discrete events resulting from both processes (see Figs. 3f and 4b for cumulative fluxes). **c**, To evaluate the power of the (normalised) minimum value of [O_2] (see Extended Data Fig. 8) as a predictor of OAEs, we plot a receiver operating characteristic (ROC) curve. The area under the curve (AUC) of 0.705 shows that the [O_2] minima in our models offer reasonably good predictive performance for OAEs in the geological record. The table summarises true negative and true positive rates for the predictor using two alternative thresholds (Methods).

References

1. H. C. Jenkyns. Cretaceous anoxic events: from continents to oceans. *Journal of the Geological Society*, 137(2):171, 1980.
2. H. C. Jenkyns. Geochemistry of oceanic anoxic events. *Geochemistry, Geophysics, Geosystems*, 11(3):Q03004, 2010.
3. T. R. Them, B. C. Gill, A. H. Caruthers, A. M. Gerhardt, D. R. Gröcke, T. W. Lyons, S. M. Marroquín, S. G. Nielsen, João P. Trabucho A., and J. D. Owens. Thallium isotopes reveal protracted anoxia during the Toarcian (Early Jurassic) associated with volcanism, carbon burial, and mass extinction. *Proceedings of the National Academy of Sciences*, 115(26):6596, 2018.
4. T. Reershemius and N. J. Planavsky. What controls the duration and intensity of ocean anoxic events in the Paleozoic and the Mesozoic? *Earth-Science Reviews*, 221:103787, 2021.
5. R. L. Larson and E. Erba. Onset of the Mid-Cretaceous greenhouse in the Barremian-Aptian: Igneous events and the biological, sedimentary, and geochemical responses. *Paleoceanography*, 14(6):663–678, 1999.
6. T. M. Gernon, T. K. Hincks, A. S. Merdith, E. J. Rohling, M. R. Palmer, G. L. Foster, C. P. Bataille, and R. D. Müller. Global chemical weathering dominated by continental arcs since the mid-Palaeozoic. *Nature Geoscience*, 14(9):690–696, 2021.
7. M. A. Arthur, S. O. Schlanger, and H. C. Jenkyns. The Cenomanian-Turonian Oceanic Anoxic Event, II. Palaeoceanographic controls on organic-matter production and preservation. *Geological Society, London, Special Publications*, 26(1):401, 1987.

8. A. Pohl, A. Ridgwell, R. G. Stockey, C. Thomazo, A. Keane, E. Vennin, and C. R. Scotese. Continental configuration controls ocean oxygenation during the Phanerozoic. *Nature*, 608(7923):523–527, 2022.
9. A. C. Kerr. Oceanic plateau formation: a cause of mass extinction and black shale deposition around the Cenomanian–Turonian boundary? *Journal of the Geological Society*, 155(4):619–626, 1998.
10. S. C. Turgeon and R. A. Creaser. Cretaceous oceanic anoxic event 2 triggered by a massive magmatic episode. *Nature*, 454(7202):323–326, 2008.
11. R. E. Ernst. *Large igneous provinces*. Cambridge University Press, 2014.
12. T. M. Gernon, S. M. Jones, S. Brune, T. K. Hincks, M. R. Palmer, J. C. Schumacher, R. M. Primiceri, M. Field, W. L. Griffin, S. Y. O'Reilly, D. Keir, C. J. Spencer, A. S. Merdith, and A. Glerum. Rift-induced disruption of cratonic keels drives kimberlite volcanism. *Nature*, 620(7973):344–350, 2023.
13. T. M. Gernon, T. K. Hincks, S. Brune, S. M. Jones, D. Keir, J. Braun, A. Cunningham, and A. Glerum. Co-evolution of craton margins and interiors during continental breakup. *Nature*, accepted, in press, 2024.
14. T. M. Gernon, T. K. Hincks, T. Tyrrell, E. J. Rohling, and M. R. Palmer. Snowball Earth ocean chemistry driven by extensive ridge volcanism during Rodinia breakup. *Nature Geoscience*, 9:242–248, 2016.
15. F. Horton. Did phosphorus derived from the weathering of large igneous provinces fertilize the Neoproterozoic ocean? *Geochemistry, Geophysics, Geosystems*, 16(6):1723–1738, 2015.
16. T. Tyrrell. The relative influences of nitrogen and phosphorus on oceanic primary production. *Nature*, 400(6744):525–531, 1999.
17. F. Zhang, S. J. Romaniello, T. J. Algeo, K. V. Lau, M. E. Clapham, S. Richoz, A. D. Herrmann, H. Smith, M. Horacek, and A. D. Anbar. Multiple episodes of extensive marine anoxia linked to global warming and continental weathering following the latest permian mass extinction. *Science Advances*, 4(4):e1602921, 2018.
18. L. M. E. Percival, E. Ownsworth, S. A. Robinson, D. Selby, S. Goderis, and P. Claeys. Valanginian climate cooling and environmental change driven by Paraná-Etendeka basalt erosion. *Geology*, 51(8):753–757, 2023.
19. I. Tsandev and C. P. Slomp. Modeling phosphorus cycling and carbon burial during Cretaceous Oceanic Anoxic Events. *Earth and Planetary Science Letters*, 286(1):71–79, 2009.
20. S. Beil, W. Kuhnt, A. Holbourn, F. Scholz, J. Oxmann, K. Wallmann, J. Lorenzen, M. Aquit, and E. H. Chellai. Cretaceous oceanic anoxic events prolonged by phosphorus cycle feedbacks. *Climate of the Past*, 16(2):757–782, 2020.
21. H. P. Mort, T. Adatte, K. B. Föllmi, G. Keller, P. Steinmann, V. Matera, Z. Berner, and D. Stüben. Phosphorus and the roles of productivity and nutrient recycling during oceanic anoxic event 2. *Geology*, 35(6):483–486, 2007.
22. F. M. Monteiro, R. D. Pancost, A. Ridgwell, and Y. Donnadieu. Nutrients as the dominant control on the spread of anoxia and euxinia across the Cenomanian-Turonian oceanic anoxic event (OAE2): Model-data comparison. *Paleoceanography*, 27(4):PA4209, 2012.
23. T. D. Herbert, C. A. Dalton, Z. Liu, A. Salazar, W. Si, and D. S. Wilson. Tectonic degassing drove global temperature trends since 20 Ma. *Science*, 377(6601):116–119, 2022.

24. J. M Hayes and J. R Waldbauer. The carbon cycle and associated redox processes through time. *Philosophical Transactions of the Royal Society B: Biological Sciences*, 361(1470):931–950, 2006.
25. S. Planke, P. A. Symonds, E. Alvestad, and J. Skogseid. Seismic volcanostratigraphy of large-volume basaltic extrusive complexes on rifted margins. *Journal of Geophysical Research*, 105:19335–19351, 2000.
26. R. D. Müller, J. Cannon, X. Qin, R. J. Watson, M. Gurnis, S. Williams, T. Pfaffelmoser, M. Seton, S. H. J. Russell, and S. Zahirovic. GPlates: Building a virtual Earth through deep time. *Geochemistry, Geophysics, Geosystems*, 19(7):2243–2261, 2018.
27. T. Nozaki, Y. Kato, and K. Suzuki. Late Jurassic ocean anoxic event: evidence from voluminous sulphide deposition and preservation in the Panthalassa. *Scientific Reports*, 3(1):1889, 2013.
28. H. Matsumoto, R. Coccioni, F. Frontalini, K. Shirai, L. Jovane, R. Trindade, J. F. Savian, M. L. G. Tejada, S. Gardin, and J. Kuroda. Long-term Aptian marine osmium isotopic record of Ontong Java Nui activity. *Geology*, 49(9):1148–1152, 2021.
29. C. M. Ostrander, J. D. Owens, and S. G. Nielsen. Constraining the rate of oceanic deoxygenation leading up to a Cretaceous Oceanic Anoxic Event (OAE-2: ~94 Ma). *Science Advances*, 3(8):e1701020, 2017.
30. P. B. Kelemen and W. S. Holbrook. Origin of thick, high-velocity igneous crust along the U.S. East Coast Margin. *Journal of Geophysical Research: Solid Earth*, 100(B6):10077–10094, 1995.
31. T. M. Gernon, R. Barr, J. G. Fitton, T. K. Hincks, D. Keir, J. Longman, A. S. Merdith, R. N. Mitchell, and M. R. Palmer. Transient mobilization of subcrustal carbon coincident with Palaeocene–Eocene Thermal Maximum. *Nature Geoscience*, 15(7):573–579, 2022.
32. S. Sharoni and I. Halevy. Rates of seafloor and continental weathering govern Phanerozoic marine phosphate levels. *Nature Geoscience*, 16(1):75–81, 2023.
33. S. Brune, S. E. Williams, N. P. Butterworth, and R. D. Müller. Abrupt plate accelerations shape rifted continental margins. *Nature*, 536(7615):201–204, 2016.
34. T. M. Lenton, S. J. Daines, and B. J. W. Mills. COPSE reloaded: An improved model of biogeochemical cycling over Phanerozoic time. *Earth-Science Reviews*, 178:1–28, 2018.
35. H. C. Jenkyns, A. J. Dickson, M. Ruhl, and S. H. J. M. van den Boorn. Basalt-seawater interaction, the Plenus Cold Event, enhanced weathering and geochemical change: deconstructing Oceanic Anoxic Event 2 (Cenomanian–Turonian, Late Cretaceous). *Sedimentology*, 64(1):16–43, 2017.
36. J. Tinker, M. de Wit, and R. Brown. Mesozoic exhumation of the southern Cape, South Africa, quantified using apatite fission track thermochronology. *Tectonophysics*, 455(1):77–93, 2008.
37. J. R. Stanley, J. Braun, G. Baby, F. Guillocheau, C. Robin, R. M. Flowers, R. Brown, M. Wildman, and R. Beucher. Constraining plateau uplift in southern Africa by combining thermochronology, sediment flux, topography, and landscape evolution modeling. *Journal of Geophysical Research: Solid Earth*, 126(7):e2020JB021243, 2021.
38. J. Hu, L. Liu, M. Faccenda, Q. Zhou, K. M. Fischer, S. Marshak, and C. Lundstrom. Modification of the Western Gondwana craton by plume–lithosphere interaction. *Nature Geoscience*, 11(3):203–210, 2018.

39. J. R. Stanley, R. M. Flowers, and D. R. Bell. Erosion patterns and mantle sources of topographic change across the southern African Plateau derived from the shallow and deep records of kimberlites. *Geochemistry, Geophysics, Geosystems*, 16(9):3235–3256, 2015.

40. L. Burgener, E. Hyland, B. J. Reich, and C. Scotese. Cretaceous climates: Mapping paleo-Köppen climatic zones using a Bayesian statistical analysis of lithologic, paleontologic, and geochemical proxies. *Palaeogeography, Palaeoclimatology, Palaeoecology*, 613:111373, 2023.

41. V. P. Wright. The mantle, CO_2 and the giant Aptian chemogenic lacustrine carbonate factory of the South Atlantic: Some carbonates are made, not born. *Sedimentology*, 69(1):47–73, 2022.

42. C. P. Slomp and P. Van Cappellen. The global marine phosphorus cycle: sensitivity to oceanic circulation. *Biogeosciences*, 4(2):155–171, 2007.

43. L. J. Alcott, B. J. W. Mills, and S. W. Poulton. Stepwise Earth oxygenation is an inherent property of global biogeochemical cycling. *Science*, 366(6471):1333–1337, 2019.

44. R. Tostevin and B. J. W. Mills. Reconciling proxy records and models of Earth's oxygenation during the Neoproterozoic and Palaeozoic. *Interface Focus*, 10(4):20190137, 2020.

45. B. J. W. Mills, A. J. Krause, I. Jarvis, and B. D. Cramer. Evolution of atmospheric O_2 through the Phanerozoic, revisited. *Annual Review of Earth and Planetary Sciences*, 51(1):253–276, 2023.

46. T. R. Them II, J. D. Owens, S. M. Marroquín, A. H. Caruthers, J. P. Trabucho Alexandre, and B. C. Gill. Reduced marine molybdenum inventory related to enhanced organic carbon burial and an expansion of reducing environments in the Toarcian (Early Jurassic) Oceans. *AGU Advances*, 3(6):e2022AV000671, 2022.

47. L. M. E. Percival, A. S. Cohen, M. K. Davies, A. J. Dickson, S. P. Hesselbo, H. C. Jenkyns, M. J. Leng, T. A. Mather, M. S. Storm, and W. Xu. Osmium isotope evidence for two pulses of increased continental weathering linked to Early Jurassic volcanism and climate change. *Geology*, 44(9):759–762, 2016.

48. S. M. Stanley. Relation of Phanerozoic stable isotope excursions to climate, bacterial metabolism, and major extinctions. *Proceedings of the National Academy of Sciences*, 107(45):19185–19189, 2010.

49. W.W.L. Cheung J.G. Kairo J. Arístegui V.A. Guinder R. Hallberg N. Hilmi N. Jiao M.S. Karim L. Levin S. O'Donoghue S.R. Purca Cuicapusa B. Rinkevich T. Suga A. Tagliabue P. Williamson Bindoff, N.L. Changing Ocean, Marine Ecosystems, and Dependent Communities. In H.-O. Pörtner, D.C. Roberts, V. Masson-Delmotte, P. Zhai, M. Tignor, E. Poloczanska, K. Mintenbeck, A. Alegría, M. Nicolai, A. Okem, J. Petzold, B. Rama, N.M. Weyer, editor, *IPCC Special Report on the Ocean and Cryosphere in a Changing Climate*, chapter 5, pages 447–587. Cambridge University Press, Cambridge, UK and New York, NY, USA, https://doi.org/10.1017/9781009157964.007, 2019.

50. T. R. Them, B. C. Gill, A. H. Caruthers, D. R. Gröcke, E. T. Tulsky, R. C. Martindale, T. P. Poulton, and P. L. Smith. High-resolution carbon isotope records of the Toarcian Oceanic Anoxic Event (Early Jurassic) from North America and implications for the global drivers of the Toarcian carbon cycle. *Earth and Planetary Science Letters*, 459:118–126, 2017.

51. João Trabucho A., E. Tuenter, G. A. Henstra, K. J. van der Zwan, R. S. W. van de Wal, H. A. Dijkstra, and P. L. de Boer. The mid-Cretaceous North Atlantic nutrient trap: Black shales and OAEs. *Paleoceanography*, 25(4):PA4201, 2010.
52. A. S. Merdith, A. S. Collins, S. E. Williams, S. Pisarevsky, J. D. Foden, D. B. Archibald, M. L. Blades, B. L. Alessio, S. Armistead, D. Plavsa, C. Clark, and R. D. Müller. A full-plate global reconstruction of the Neoproterozoic. *Gondwana Research*, 50:84–134, 2017.
53. H. Matsumoto, R. Coccioni, F. Frontalini, K. Shirai, and J. Kuroda. Osmium isotopic evidence for eccentricity-paced increases in continental weathering during the Latest Hauterivian, Early Cretaceous. *Geochemistry, Geophysics, Geosystems*, 22(12):e2021GC009789, 2021.
54. P. C. Davidson, A. A. P. Koppers, T. Sano, and T. Hanyu. A younger and protracted emplacement of the Ontong Java Plateau. *Science*, 380(6650):1185–1188, 2023/09/14 2023.
55. P. G. Falkowski, M. E. Katz, A. J. Milligan, K. Fennel, B. S. Cramer, M. P. Aubry, R. A. Berner, M. J. Novacek, and W. M. Zapol. The rise of oxygen over the past 205 million years and the evolution of large placental mammals. *Science*, 309(5744):2202–2204, 2005.
56. M. R. Saltzman and E. Thomas. *Carbon Isotope Stratigraphy*, chapter 11, pages 207–232. Elsevier, 2012.
57. J. Veizer, D. Ala, K. Azmy, P. Bruckschen, D. Buhl, F. Bruhn, G. A. F. Carden, A. Diener, S. Ebneth, Y. Godderis, T. Jasper, C. Korte, F. Pawellek, O. G. Podlaha, and H. Strauss. ^{87}Sr/^{86}Sr, δ^{13}C and δ^{18}O evolution of Phanerozoic seawater. *Chemical Geology*, 161(1):59–88, 1999.
58. A. S. Merdith, S. E. Williams, S. Brune, A. S. Collins, and R. D. Müller. Rift and plate boundary evolution across two supercontinent cycles. *Global and Planetary Change*, 173:1–14, 2019.
59. R. D. Müller, M. Seton, S. Zahirovic, S. E. Williams, K. J. Matthews, N. M. Wright, G. E. Shephard, K. T. Maloney, N. Barnett-Moore, M. Hosseinpour, D. J. Bower, and J. Cannon. Ocean basin evolution and global-scale plate reorganization events since Pangea breakup. *Annual Review of Earth and Planetary Sciences*, 44(1):107–138, 2016.

Methods

Quantitative estimation of seafloor production rates

To calculate seafloor production rates, we used the plate model of Müller et al.[59], with some corrections as outlined in Torsvik et al.[60]. This plate model comprises a digital repository of continents and plate boundaries, and, through a series of Euler rotations, tracks how they have evolved through time. For the Mesozoic–Cenozoic, they are based predominantly on the seafloor spreading history preserved in ocean basins[61].

In our analysis, we use the Python library, *pyGPlates* (gplates.org/docs/pygplates/index.html), to extract all mid-ocean ridges where seafloor spreading occurred, and their associated kinematic data, from the plate model. This includes the length of spreading segments, the rate of spreading, start and end time of activity and the reconstructed position (i.e., the latitude and longitude of the mid-ocean ridge) among other metadata. Overall seafloor production rates—that is, a measure of the area in km^2 of new seafloor formed along mid-ocean ridges per Myr—are calculated by summing the product of spreading rate and spreading segment length for each individual length of the global ridge system. We then export the entire dataset to individual .csv files for each 1 Myr time-step between 200 and 0 Ma.

Using the plate tectonic reconstruction software, *GPlates*[26] (https://www.gplates.org/), we defined bounding polygons around incipient mid-ocean ridge systems that evolved from a continental rift (i.e., in a region of thick continental lithosphere; Extended Data Fig. 1). In our model, these polygons are active for the first 30 Myr of spreading, when the incipient ridge is mostly still relatively shallow and susceptible to enhanced weathering (see main text). Nevertheless, we apply a linear decay in fragmentation and phosphorus release during seafloor subsidence (as discussed below), which accounts for reduced weathering intensity as the ridge progressively deepens in our model. Spatially, the polygons are defined around congruent geographic regions representing incipient ocean basins. These geographic regions do not always map well to present-day: for example, the opening of the Atlantic Ocean is divided into Northern, Iberian, Central, Equatorial and Southern ridge segments. The oceanic ridge systems included in our analysis, with accepted start time in brackets, are as follows: Central Atlantic (180 Ma), Australia-Molucca (155 Ma), Africa-Madagascar (154 Ma), Africa-Antarctica (154 Ma), Iberian-Atlantic (140 Ma), South Atlantic (132 Ma), India-Australia-Antarctica (131 Ma), Equatorial Atlantic (120 Ma) and India-Madagascar (87 Ma). These data are summarised in Figs. 3a–d and Extended Data Fig. 1 and are supplied in Supplementary Data File S1.

The above analysis yields a series of polygons that spatially and temporally define the limits of incipient MORs, and a series of datasets describing all active ridges at a specified time-step. We use the ‘select’ function of the Generic Mapping Tools (https://www.generic-mapping-tools.org/) software, which intersects datasets (including .csv files with latitude/ longitude co-ordinates) against a polygon(s), to extract data within the polygon at each time-step per bounding box (at their active times). This gives us individual time-series (multiple .csv files) of the ridge segments within each bounding box that we merge into individual profiles for each discrete ocean basin.

Mapping OAEs

Figure 1 plots the location of organic-rich facies and carbon isotope excursions of the two major OAEs, T-OAE and OAE 2. These locations were previously compiled by Them et al.[50] for T-OAE (building on the earlier compilation of ref.[62]), and Joaõ Trabucho et al.[51] for OAE 2. The maps were produced using the open-source plate-tectonic reconstruction software, GPlates, using the palaeogeographic regions of Cao et al.[63] and the plate rotations of Müller et al.[64]. The distribution of large igneous provinces was plotted using the shape-files of Johansson et al.[65].

Modelling shallow mid-ocean ridge phosphorus release

To estimate the flux of phosphorus into the ocean from fragmented basaltic materials emplaced along shallow incipient mid-ocean ridges (Extended Data Fig. 1), we adapted models from ref.[14], which probabilistically estimate elemental fluxes from the chemical weathering of seafloor basalts, accounting for uncertainties in parameters. Because seafloor production is reasonably well constrained for the Jurassic and Cretaceous[59,66], we used seafloor production data (acquired using the above procedures) in our models. These data include estimates for seafloor production rates (km^2 Myr^{-1}), total ridge length (km), and mean spreading rate (km Myr^{-1}) globally at 1 Myr intervals. The nine ridges considered in this analysis, listed above (Figs. 3a,d), are shown in Extended Data Fig. 1 (Supplementary Data File 1). We define ‘shallow’ as water depths of 1,500 m or less. We also consider durations for ridge productivity of up to 30 Myr after ridge initiation, a period during which the ridge should be at its shallowest[67,68], particularly in the presence of dynamic support. To account for age uncertainty associated with the timing of ridge formation, we apply a random offset to the start time (t_s) of each ridge (Fig. 3e), sampling from a Beta distribution scaled to the interval [0 , 0.05t_s]. This approach simulates uncertainty that increases further back in time[6], up to 5% of t_s. We use Beta parameters α=1, β=1.5 (skewed towards zero), which corresponds to a mean offset of 2%, and standard deviation of approximately 1.3%.

Our model estimates the volume of fragmental basaltic material over time for each rift/ridge segment (see main text). We assume that the total thickness of this material formed and accessed by seawater infiltration will decrease over the duration considered in the model runs. This assumption is considered reasonable because: (1) higher magmatic productivity is expected at the earliest stages during ridge initiation due to decompression melting and active upwelling of asthenosphere[31,30,69], which typically coincides with (2) initially shallow water conditions that favour more intense hydrovolcanism (e.g., hyaloclastite formation)[25] and pyroclastic eruptions[14]; (3) when new seafloor subsides and is transported away from the ridge it cools and is expected to experience less vigorous convection by infiltrating seawater and hydrothermal flow processes[70,71]. Therefore, we simulate a simple linear decay in thickness of fragmental material over time, from 1,500 metres to 100 m over the model run, values which are considered realistic based on observations of seafloor hydrothermal systems[14,70]. We apply ranges of values for shallow and deep porosity, hyaloclastite abundance, and palagonite fraction[72] used in previous models[14]. We also used element loss estimates from ref.[14], based on ref.[72] (Extended Data Fig. 2), yielding the following uniform distributions: P_2O_5 loss: [0.002, 0.006]. In our calculations, we use a standard density of 2,390 kg m^{-3} for P_2O_5.

We performed 10,000 individual calculations to build up an output distribution that captures the estimated uncertainty in model parameters and timing of ridge initiation. For each iteration, we step through each ridge in turn, sampling palagonite fraction, shallow/deep porosity, hyaloclastite fraction, and element losses (specifically, in our case, P_2O_5). Then, for each ridge, we step through the active period at 1 Myr time intervals. At each timestep from t=0 (when the ridge first becomes active) we use the ridge production values and alteration depth (using the linear decay model) from the input file. The absolute event timing is modified for each ridge at each iteration using a sampled offset (explained above), and the time-series are finally interpolated to regular 1 Myr intervals before being combined with the results from all ridges and model iterations.

We next calculated hyaloclastite thickness as a function of alteration depth and sampled hyaloclastite fractions. By multiplying hyaloclastite thickness by ridge production, we then calculate the total hyaloclastite volume, and hyaloclastite weight. The total weight of P_2O_5 released is the weight of hyaloclastite, multiplied by the randomly sampled palagonite fraction and P_2O_5 loss (using the distributions given above). We then convert to moles P, as a total flux into the ocean per 1 Myr.

This procedure gives 10,000 individual (offset) time series for P for each ridge. We performed linear interpolation of each (offset) time series to estimate the total P (mol) released from each ridge at regular 1 Myr time-steps, from 180 Ma to 59 Ma (Extended Data Fig. 3). Then, for each individual iteration, we calculated the total mol P from all active ridges. This gives 10,000 variant time-series for total estimated mol P. From this we can then calculate the mean, median, and percentile estimates at each time step (5, 10, 90 and 95th percentile mol P). The resulting time series for mol P, and associated uncertainty, is shown in Fig. 3f. These data are supplied in Supplementary Data File S2.

Modelling continental denudation

In addition to incipient mid-ocean ridges, we simulate the phosphorus contribution from a major phase of uplift and denudation that occurred across southern Africa from about 160 Ma to 80 Ma (see main text). This denudation involved basaltic lavas of the c. 183 Ma Karoo Group[73]. The present-day Drakensberg Mountains in Lesotho are a relic of this thick basaltic sequence, which during the Cretaceous Period, extended much farther to the west[39]. We sought to quantitatively estimate the amount of P liberated during chemical denudation of these basalts in this interval. To do this, we turned to thermochronology, which provides constraints on the spatial and temporal extent and magnitude of crustal cooling and thus exhumation (i.e., uplift and denudation). These cooling history models[39,36,37,74,75,76,77,78,79,80,81] cover a large area of southern Africa owing to the availability of well-dated kimberlite pipes.

We used the rate of change of temperature (i.e., cooling rates) from prior thermochronology studies for 28 individual localities spanning southern Africa, using 'best fit' thermal histories defined in those studies[13]. These are temporally irregularly spaced observations/measurements, so we interpolate to give regular time series with a 0.1 Myr interval (a linear interpolation using the R *approx()* function). We extend all time series to span the period 160 to 55 Ma, using the first and last observed values to pad the series as required.

For each locality we use the R function *rollapply()* to calculate the change in temperature T over a 1.9 Myr symmetric (rectangular) moving window:

$$\Delta T/\Delta t_{1.9Myr(t)} = \frac{(T(t-0.9) - T(t+0.9))}{1.9}$$

This is the estimated temperature drop occurring at time t, over the window t ± 0.9 Myr. Note that the total width is an odd number as we require a symmetric window. At each 0.1 Myr time step, t (from 160 Ma to 55 Ma), we then find the maximum value of $\Delta T/\Delta t_{1.9Myr}$ over all the localities and save this as a separate time series (*max(f(t))*, where *f(t)* = maximum temperature drop over all localities at a given time step, t). This is then used to estimate the denudation rate and quantitatively compute how this varies over time.

We assume a minimum denudation rate D_{min} = 20 m Myr^{-1}, and maximum rate D_{max} = 175 m Myr^{-1}, based on previously reported denudation rates in this region spanning this interval, and underpinned by thermochronology and offshore sediment accumulation histories[36]. We make the simplifying assumption that the denudation rate scales linearly with the rate of temperature drop — the estimated maximum ΔT at each time step. This means we have a denudation rate D = 20 m Myr^{-1} where ΔT is at its minimum ($\min_{\Delta T}$= min(f), over the period of interest) and a denudation rate D = 175 m Myr^{-1} where ΔT is at its maximum, $\max_{\Delta T}$=max(f). The scaling factor S_D for denudation is then computed as follows:

$$Dscale(t) = \frac{(f(t) - min_{\Delta T})}{(max_{\Delta T} - min_{\Delta T})}$$

$$Denudation, D = D_{min} + (S_D \cdot (Dmax - Dmin))$$

$$Eroded_{vol(t)} = Basalt_{area} \cdot (Denudation(t)/1000)$$

The variable *Basalt_area* denotes the spatial extent of basalts the Drakensberg Group. This area is estimated as 600,000 km^2 based on thermochronology models[39,74], fragments of basalt preserved in deeply eroded kimberlite pipes[82], and the present-day spatial footprint of intrusions that served as feeders to flood basalt eruptions[73] (Fig. 4a). We convert denudation rate from m Myr^{-1} to to km Myr^{-1} to give the total volume in km^3 Myr^{-1}. We can then estimate how much phosphorous this potentially involves.

To estimate P_2O_5 contents of the weathered basalts, we sample from a large database, obtained from the GeoRoc repository (https://georoc.eu/), of measured P_2O_5 contents from basalts of the Karoo and age equivalent Ferrar Provinces. We used this dataset as an empirical distribution for P_2O_5 in our models instead of fitting an arbitrary distribution. We performed 10,000 iterations to build up an output distribution for output P (Mol) over time. The P_2O_5 data set has a total of 2,495 observations (latitude, longitude and P_2O_5 content as a percentage, ranging from >0 to 5.39%), and we exclude a small number of cases (36) with zero P_2O_5 contents. The estimated phosphorus fluxes from each of the nine continental weathering ‘events’ considered are supplied in Supplementary Data File S3.

Biogeochemical modelling of the effects of P inputs

To test the effects of P input into the ocean through incipient seafloor ridges and continental basaltic weathering, we use the 5-box ocean-atmosphere model of Alcott et al.[43]. The model tracks the long-term evolution of the carbon, phosphorus, and oxygen cycles over Earth history, and was extended from a model originally developed to investigate Mesozoic OAEs[42]. In this study, we use the standard run of the model but impose phosphorus input events based on our data compilation for ocean ridges (Fig. 3) and continental denudation events (Fig. 4). We include the sluggish open ocean upwelling based on previous uses of this model to investigate OAEs[42]. P input from ridges is delivered into the ‘Deep ocean’ box as soluble reactive phosphorus. P input from weathering is delivered into the ‘Proximal zone’ box of the continental margin, again as soluble reactive phosphorus (Extended Data Fig. 5). We track the model response to these input forcings by plotting the deep ocean [O_2] concentration (Figs. 5a–b; Extended Data Fig. 7; Supplementary Data S4). Although we produce estimates of the combined P inputs over the Mesozoic, we test each input event in the model individually. This is because the model lacks powerful feedbacks on atmospheric oxygen levels associated with the land biosphere, and thus combined long-term increases in P inputs can raise atmospheric O_2 to high levels which are no longer consistent with a Mesozoic background state.

Evaluating the predictive performance of biogeochemical models

Here, we outline the methodology used to assess the predictive power of the minimum value of [O_2] in our biogeochemical models (Fig. 5) as an indicator for the timing of OAEs in the geological record (Extended Data Table 1). To generate a single predictive measure from separate model runs, we first computed the mean output for the weathering and individual ridge model simulations (Fig. 5; note each ridge is simulated separately). At each time step, we identified the overall minimum value of [O_2], selecting the lowest value either from the ridge model (Fig. 5a) or the riverine/weathering model (Fig. 5b). This allows us to derive a single measure from multiple, separate model runs (Extended Data Fig. 8a), mitigating the need to use arbitrary thresholds to define “lows” in [O_2] levels.

We then normalised this derived time series (Extended Data Fig. 8a) to the interval [0,1] and inverted the values (1 – normalised value). This yields a simple predictor for OAE events (that is, a binary outcome), allowing us to test the hypothesis that values closer to 1 (corresponding to the [O_2] minima) indicate a higher probability of OAE occurrence. This normalised and inverted time series is shown in Extended Data Fig. 8b.

To evaluate the predictive performance of this model, we plotted a Receiver Operating Characteristic (ROC) curve (Fig. 5c), which shows the trade-off between sensitivity (the true positive rate, i.e., the probability of predicting an OAE event given an actual OAE event) and specificity (the true negative rate, correctly predicting the absence of an OAE event) for a range of classification thresholds. The area under the curve (AUC) provides a measure of the forecast performance: that is, a random, no-skill forecast would follow the diagonal line with an AUC of 0.5, and a perfect classifier would have an AUC of 1 (perfect sensitivity and specificity). The 95% confidence intervals are computed from 2,000 stratified bootstrap samples using the R package, *pROC*[83] (CRAN.R-project.org/package=pROC). The ROC plot (Fig. 5c) shows that the simple classifier (described above) derived from modelled [O_2] minima (Extended Data Fig. 8) is a reasonably good predictor of OAEs in the geological record, surpassing random chance.

Two examples of potential diagnostic thresholds are given in Fig. 5c (corresponding to Extended Data Fig. 8). Youden's J statistic[84] (red text/line) defines the optimal cut-off as the threshold value that maximises the distance to the diagonal. "Closest to top left" (blue) minimises the distance from the top left corner (the point corresponding to perfect sensitivity and specificity). Classifier values over a given threshold correspond to a prediction of an OAE event occurring, and values below the threshold predict no OAE.

As shown in the inset table of Fig. 5c, using the threshold 0.19 gives a true positive rate (TPR) of 0.71; this is higher than using the Youden method (TPR 0.625), but at a cost of a lower true negative rate (TNR 0.70 vs. 0.79 for the Youden method). In practice the relative cost of a false alarm or miss would be evaluated to determine the optimal threshold.

Extended Data References

Additional references are cited in Extended Data[85,86].

Additional references cited in Extended Data Table 1:

During the preparation of this paper, we used the ICS International Chronostratigraphic Chart published in 2022/10[87]. Additional references cited in Extended Data Table 1 are: Mattioli et al. (2014)[88]; Wouters et al. (2018)[89]; Rodríguez-Tovar & Uchman (2017)[90]; Jenkyns (2018)[91]; Leckie et al. (2002)[92]; Millán et al. (2014)[93]; Friedrich et al. (2018)[94]; Núñez-Useche et al. (2014)[95], and Kouamelan et al. (2020)[96].

Additional references cited in Extended Data Table 2:

Composite record of ^{187}Os/^{188}Os$_i$ during the Mesozoic (see Extended Data Table 2), incorporating data from the studies of Them et al.[97], Percival et al. (2016)[98], Lu et al.[99], Matsumoto et al. (2021a)[53], Matsumoto et al. (2021b)[28] (which includes data from Matsumoto et al.[100] and Tejada et al.[101]), Matsumoto et al. (2022)[102], Sullivan et al.[103], Percival et al. (2020)[104] (also used to supplement the δ^{13}C record for OAE 2 in Fig. 2c), Jones et al.[105], De Lena et al.[106], and Porter et al. (2013)[107] and Porter et al. (2014)[108]. Note that the compilation of ^{187}Os/^{188}Os$_i$ from Matsumoto et al. (2022)[102] includes data from Turgeon and Creaser[10], Tejada et al.[101], Bottini et al.[109], Matsumoto et al.[28,100] and Percival et al.[110].

Data availability

All data generated or analysed during this study are provided in Source Data Files and Extended Data Tables 1–2. All model outputs are available via Figshare at: https://doi.org/10.6084/m9.figshare.24153351.

Code availability

The computational codes used for the plate tectonic modelling is available at GitHub via the following link: https://github.com/amer7632/Gernon_OAE_workflows. The code for the biogeochemical models available at GitHub via the following link: https://github.com/bjwmills/Gernon2024.

References

60. T. H. Torsvik, B. Steinberger, G. E. Shephard, P. V. Doubrovine, C. Gaina, M. Domeier, C. P. Conrad, and W. W. Sager. Pacific-Panthalassic reconstructions: Overview, errata and the way forward. *Geochemistry, Geophysics, Geosystems*, 20(7):3659–3689, 2019.
61. M. Seton, R. D. Müller, S. Zahirovic, C. Gaina, T. Torsvik, G. Shephard, A. Talsma, M. Gurnis, M. Turner, S. Maus, and M. Chandler. Global continental and ocean basin reconstructions since 200 Ma. *Earth-Science Reviews*, 113(3):212–270, 2012.
62. H. C. Jenkyns. The early Toarcian (Jurassic) anoxic event; stratigraphic, sedimentary and geochemical evidence. *American Journal of Science*, 288(2):101–151, 1988.
63. W. Cao, S. Zahirovic, N. Flament, S. Williams, J. Golonka, and R. D. Müller. Improving global paleogeography since the late Paleozoic using paleobiology using paleobiology. *Biogeosciences*, 14(23):5425–5439, 2017.
64. R. D. Müller, S. Zahirovic, S. E. Williams, J. Cannon, M. Seton, D. J. Bower, M. G. Tetley, C. Heine, E. Le Breton, S. Liu, S. H. J. Russell, T. Yang, J. Leonard, and M. Gurnis. A global plate model including lithospheric deformation along major rifts and orogens since the Triassic. *Tectonics*, 38(6):1884–1907, 2019.
65. L. Johansson, S. Zahirovic, and R. D. Müller. The interplay between the eruption and weathering of large igneous provinces and the deep-time carbon cycle. *Geophysical Research Letters*, 45(11):5380–5389, 2018.
66. R. D. Müller, M. Sdrolias, C. Gaina, and W. R. Roest. Age, spreading rates, and spreading asymmetry of the world's ocean crust. *Geochemistry, Geophysics, Geosystems*, 9(4):1–19, 2008.
67. B. Parsons and J. G. Sclater. An analysis of the variation of ocean floor bathymetry and heat flow with age. *Journal of Geophysical Research*, 82(5):803–827, 1977.
68. J. R. Cochran and W. R. Buck. Near-axis subsidence rates, hydrothermal circulation, and thermal structure of mid-ocean ridge crests. *Journal of Geophysical Research: Solid Earth*, 106(B9):19233–19258, 2001.
69. M. Storey, R. A. Duncan, and C. Tegner. Timing and duration of volcanism in the North Atlantic Igneous Province: Implications for geodynamics and links to the iceland hotspot. *Chemical Geology*, 241:264–281, 2007.
70. J. C. Alt. Subseafloor processes in mid-ocean ridge hydrothernal systems. In S. E. Humphris, R. A. Zierenberg, L. S. Mullineaux, and R.E. Thomson, editors, *Seafloor Hydrothermal Systems: Physical, Chemical, Biological, and Geological Interactions*. AGU Geophysical Monograph Series, 1995.
71. M. J. Mottl and C. G. Wheat. Hydrothermal circulation through mid-ocean ridge flanks: Fluxes of heat and magnesium. *Geochimica et Cosmochimica Acta*, 58(10):2225–2237, 1994.

72. N. A. Stroncik and H. U. Schmincke. Palagonite – a review. *International Journal of Earth Sciences*, 91:680–697, 2002.

73. Council for Geoscience. Geologic map of South Africa, 1:1M: National Science Councils of South Africa. 41 / 2236592, 2016.

74. J. R. Stanley, R. M. Flowers, and D. R. Bell. Kimberlite (U-Th)/He dating links surface erosion with lithospheric heating, thinning, and metasomatism in the southern African Plateau. *Geology*, 41(12):1243–1246, 2013.

75. R. W. Brown, M. A. Summerfield, and A. J. W. Gleadow. Denudational history along a transect across the Drakensberg Escarpment of southern Africa derived from apatite fission track thermochronology. *Journal of Geophysical Research: Solid Earth*, 107(B12), 2002.

76. J. R. Stanley and R. M. Flowers. Mesozoic denudation history of the lower Orange River and eastward migration of erosion across the southern African Plateau. *Lithosphere*, 12(1):74–87, 2020.

77. A. Kounov, G. Viola, M. de Wit, and M. A. G. Andreoli. Denudation along the Atlantic passive margin: new insights from apatite fission-track analysis on the western coast of South Africa. *Geological Society, London, Special Publications*, 324(1):287–306, 2009.

78. A. Kounov, G. Viola, I. Dunkl, and H. E. Frimmel. Southern African perspectives on the long-term morpho-tectonic evolution of cratonic interiors. *Tectonophysics*, 601:177–191, 2013.

79. M. Wildman, R. Brown, R. Watkins, A. Carter, A. Gleadow, and M. A. Summerfield. Post break-up tectonic inversion across the southwestern cape of South Africa: New insights from apatite and zircon fission track thermochronometry. *Tectonophysics*, 654:30–55, 2015.

80. M. Wildman, R. Brown, C. Persano, R. Beucher, F. M. Stuart, V. Mackintosh, K. Gallagher, J. Schwanethal, and A. Carter. Contrasting Mesozoic evolution across the boundary between on and off craton regions of the South African plateau inferred from apatite fission track and (U-Th-Sm)/He thermochronology. *Journal of Geophysical Research: Solid Earth*, 122(2):1517–1547, 2017.

81. P. F. Green, I. R. Duddy, P. Japsen, J. M. Bonow, and J. A. Malan. Post-breakup burial and exhumation of the southern margin of Africa. *Basin Research*, 29(1):96–127, 2017.

82. E. K. Hanson, J. M. Moore, E. M. Bordy, J. S. Marsh, G. Howarth, and J. V. A. Robey. Cretaceous erosion in central South Africa: Evidence from upper-crustal xenoliths in kimberlite diatremes. *South African Journal of Geology*, 112(2):125–140, 2009.

83. X. Robin, N. Turck, A. Hainard, N. Tiberti, F. Lisacek, J.-C. Sanchez, and M. Müller. pROC: an open-source package for R and S+ to analyze and compare ROC curves. *BMC Bioinformatics*, 12(1):77, 2011.

84. W. J. Youden. Index for rating diagnostic tests. *Cancer*, 3(1):32–35, 1950.

85. Z. Zhou and W. S. Fyfe. Palagonitization of basaltic glass from DSDP Site 335, Leg 37; textures, chemical composition, and mechanism of formation. *American Mineralogist*, 74(9-10):1045–1053, 1989.

86. I. C. Handoh and T. M. Lenton. Periodic mid-Cretaceous oceanic anoxic events linked by oscillations of the phosphorus and oxygen biogeochemical cycles. *Global Biogeochemical Cycles*, 17(4):1092, 2003.

87. K.M. Cohen, D.A.T. Harper, and P.L. Gibbard. ICS International Chronostratigraphic Chart 2022/10. International Commission on Stratigraphy, IUGS. www.stratigraphy.org, 2022.

88. E. Mattioli, B. Pittet, L. Riquier, and V. Grossi. The mid-Valanginian Weissert Event as recorded by calcareous nannoplankton in the Vocontian Basin. *Palaeogeography, Palaeoclimatology, Palaeoecology*, 414:472–485, 2014.

89. S. Wouters, J. Schnyder, S. Satolli, M. Martinez, F. Boulvain, T. Goovaerts, B. Meyvis, and X. Devleeschouwer. Progressive increase in organic-matter burial and preservation from the “Weissert” event to the Faraoni event in Umbria-Marche (central Italy). In *6th International Geologica Belgica Meeting*. KU Leuven, 2018.

90. F. J. Rodríguez-Tovar and A. Uchman. The Faraoni event (latest Hauterivian) in ichnological record: The Río Argos section of southern Spain. *Cretaceous Research*, 79:109–121, 2017.

91. H. C. Jenkyns. Transient cooling episodes during Cretaceous Oceanic Anoxic Events with special reference to OAE 1a (Early Aptian). *Philosophical Transactions of the Royal Society A: Mathematical, Physical and Engineering Sciences*, 376(2130):20170073, 2018.

92. R. M. Leckie, T. J. Bralower, and R. Cashman. Oceanic anoxic events and plankton evolution: Biotic response to tectonic forcing during the mid-Cretaceous. *Paleoceanography*, 17(3):13–1–13–29, 2002.

93. M. I. Millán, H. J. Weissert, and M. A. López-Horgue. Expression of the late Aptian cold snaps and the OAE1b in a highly subsiding carbonate platform (Aralar, northern Spain). *Palaeogeography, Palaeoclimatology, Palaeoecology*, 411:167–179, 2014.

94. O. Friedrich, A. Bornemann, R. D. Norris, J. Erbacher, and J. Fiebig. Changes in tropical Atlantic surface-water environments inferred from late Albian planktic foraminiferal assemblages (ODP Site 1258, Demerara Rise). *Cretaceous Research*, 87:74–83, 2018.

95. F. Núñez-Useche, R. Barragán, J. A. Moreno-Bedmar, and C. Canet. Mexican archives for the major Cretaceous Oceanic Anoxic Events. *Boletín de la Sociedad Geológica Mexicana*, 66(3):491–505, 2014.

96. K. S. Kouamelan, C. Zou, C. Wang, K. R. Assie, C. Peng, O. R. Mondah, K. A. N’dri, and E. T. Brantson. Multifractal characterization of the Coniacian–Santonian OAE3 in lacustrine and marine deposits based on spectral gamma ray logs. *Scientific Reports*, 10(1):14363, 2020.

97. T. R. Them, B. C. Gill, D. Selby, D. R. Gröcke, R. M. Friedman, and J. D. Owens. Evidence for rapid weathering response to climatic warming during the Toarcian Oceanic Anoxic Event. *Scientific Reports*, 7(1):5003, 2017.

98. L. M. E. Percival, A. S. Cohen, M. K. Davies, A. J. Dickson, S. P. Hesselbo, H. C. Jenkyns, M. J. Leng, T. A. Mather, M. S. Storm, and W. Xu. Osmium isotope evidence for two pulses of increased continental weathering linked to Early Jurassic volcanism and climate change. *Geology*, 44(9):759–762, 2016.

99. X. Lu, B. Kendall, H. J. Stein, and J. L. Hannah. Temporal record of osmium concentrations and ^{187}Os/^{188}Os in organic-rich mudrocks: Implications for the osmium geochemical cycle and the use of osmium as a paleoceanographic tracer. *Geochimica et Cosmochimica Acta*, 216:221–241, 2017.

100. H. Matsumoto, J. Kuroda, R. Coccioni, F. Frontalini, S. Sakai, N. O. Ogawa, and N. Ohkouchi. Marine Os isotopic evidence for multiple volcanic episodes during Cretaceous Oceanic Anoxic Event 1b. *Scientific Reports*,

10(1):12601, 2020.

101. M. L. G. Tejada, K. Suzuki, J. Kuroda, R. Coccioni, J. J. Mahoney, N. Ohkouchi, T. Sakamoto, and Y. Tatsumi. Ontong Java Plateau eruption as a trigger for the early Aptian oceanic anoxic event. *Geology*, 37(9):855–858, 2009.
102. H. Matsumoto, R. Coccioni, F. Frontalini, K. Shirai, L. Jovane, R. Trindade, J. F. Savian, and J. Kuroda. Mid-Cretaceous marine Os isotope evidence for heterogeneous cause of oceanic anoxic events. *Nature Communications*, 13(1):239, 2022.
103. D. L. Sullivan, A. D. Brandon, J. Eldrett, S. C. Bergman, S. Wright, and D. Minisini. High resolution osmium data record three distinct pulses of magmatic activity during Cretaceous Oceanic Anoxic Event 2 (OAE-2). *Geochimica et Cosmochimica Acta*, 285:257–273, 2020.
104. L. M. E. Percival, N. A. G. M. van Helmond, D. Selby, S. Goderis, and P. Claeys. Complex interactions between large igneous province emplacement and global-temperature changes during the Cenomanian-Turonian Oceanic Anoxic Event (OAE 2). *Paleoceanography and Paleoclimatology*, 35(10):e2020PA004016, 2020.
105. M. M. Jones, D. E. Ibarra, Y. Gao, B. B. Sageman, D. Selby, C. P. Chamberlain, and S. A. Graham. Evaluating Late Cretaceous OAEs and the influence of marine incursions on organic carbon burial in an expansive East Asian paleo-lake. *Earth and Planetary Science Letters*, 484:41–52, 2018.
106. L. F. De Lena, D. Taylor, J. Guex, A. Bartolini, T. Adatte, D. van Acken, J. E. Spangenberg, E. Samankassou, T. Vennemann, and U. Schaltegger. The driving mechanisms of the carbon cycle perturbations in the late Pliensbachian (Early Jurassic). *Scientific Reports*, 9(1):18430, 2019.
107. S. J. Porter, D. Selby, K. Suzuki, and D. Gröcke. Opening of a trans-Pangaean marine corridor during the Early Jurassic: Insights from osmium isotopes across the Sinemurian–Pliensbachian GSSP, Robin Hood's Bay, UK. *Palaeogeography, Palaeoclimatology, Palaeoecology*, 375:50–58, 2013.
108. S. J. Porter, P. L. Smith, A. H. Caruthers, P. Hou, D. R. Gröcke, and D. Selby. New high resolution geochemistry of Lower Jurassic marine sections in western North America: A global positive carbon isotope excursion in the Sinemurian? *Earth and Planetary Science Letters*, 397:19–31, 2014.
109. C. Bottini, A. S. Cohen, E. Erba, H. C. Jenkyns, and A. L. Coe. Osmium-isotope evidence for volcanism, weathering, and ocean mixing during the early Aptian OAE 1a. *Geology*, 40(7):583–586, 2012.
110. L. M. E. Percival, L. R. Tedeschi, R. A. Creaser, C. Bottini, E. Erba, F. Giraud, H. Svensen, J. Savian, R. Trindade, R. Coccioni, F. Frontalini, L. Jovane, T. A. Mather, and H. C. Jenkyns. Determining the style and provenance of magmatic activity during the Early Aptian Oceanic Anoxic Event (OAE 1a). *Global and Planetary Change*, 200:103461, 2021.

Supplementary Data

Supplementary Data File S1:

Seafloor production rates along nine nascent mid-ocean ridge systems identified in the study. Data files are provided for each ridge individually (for labels, see Fig. 3 and Extended Data Fig. 1) and for the global total production rates at each time step from 180 Ma to 10 Ma. The files provide columns for the age in Ma, seafloor production in km^2, ridge length in km, and mean spreading rate in km Myr^{-1}.

Supplementary Data File S2:

Modelled phosphorus release (in mol yr^{-1}) from each of the mid-ocean ridge systems (see Fig. 3), based on production rates provided in Supplementary Data S1 (see Methods for details). Data files are provided for each ridge individually (as shown in Extended Data Fig. 3) and for the global total flux (as shown in Fig. 3f). The files provide columns for the age in Ma (negative), mean and median P flux, min and max P flux, and the 5th, 10th, 90th and 95th percentile values.

Supplementary Data File S3:

Modelled phosphorus fluxes (in mol yr^{-1}) from subaerial weathering events tied to substantial exhumation of basalts in southern Africa, the criteria for which are described in the Methods. Data are provided for 10 discrete events, combined in Fig. 4d. Each file provides columns for the age in Ma (negative), mean and median P flux, min and max P flux, and the 1st, 5th, 10th, 90th, 95th and 99th percentile values.

Supplementary Data File S4:

Outputs from our biogeochemical models for ridge formation events (R1 to R9) and continental basalt weathering events (W1 to W9). These data are used to plot the minimum [O_2] distributions shown in Figures 5a and 5b.

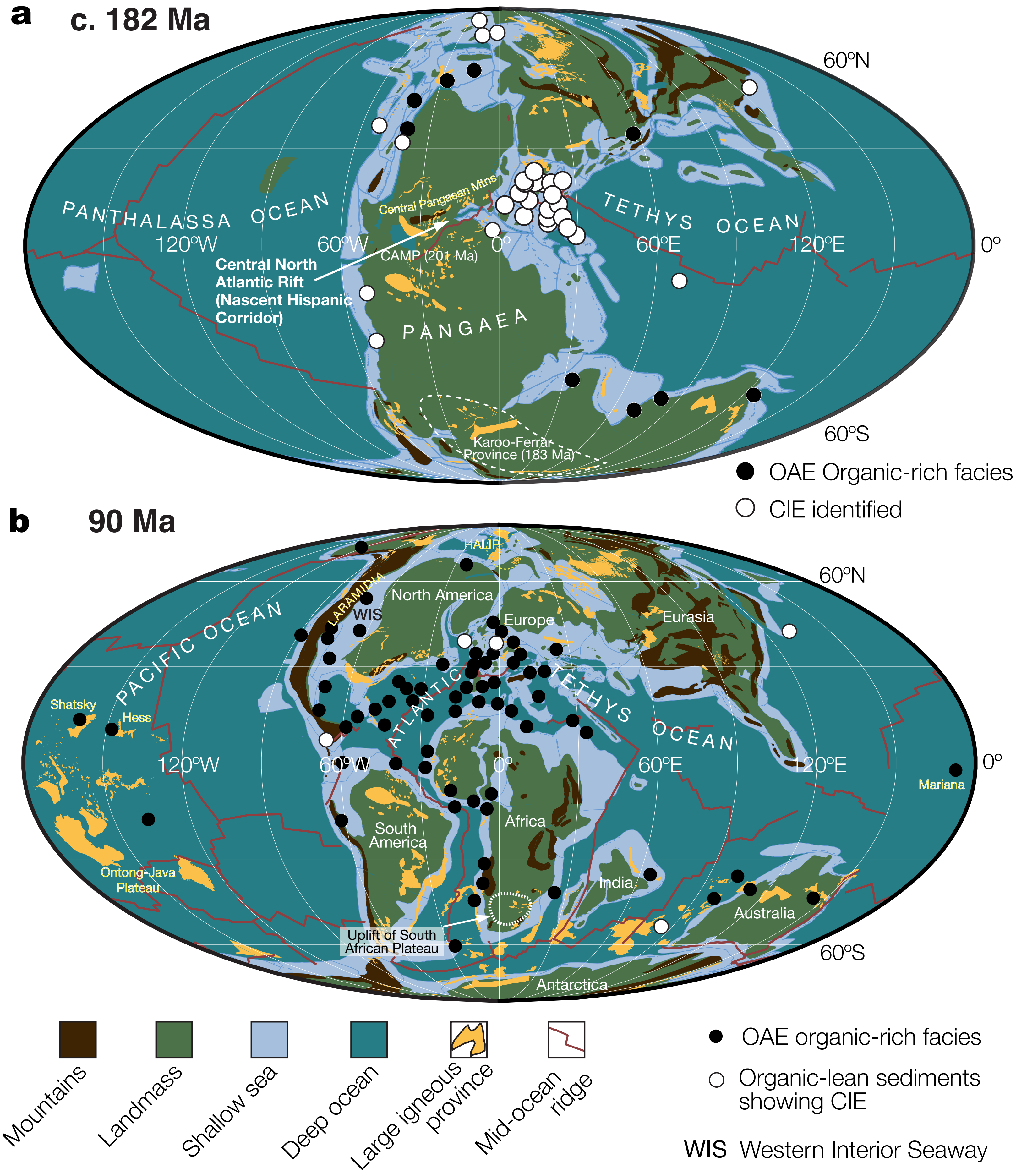
a
c. 182 Ma
60ºN
PANTHALASSA OCEAN
TETHYS OCEAN
Central Pangaean Mtns
120ºW
60ºW
0º
60ºE
120ºE
0º
CAMP (201 Ma)
Central North Atlantic Rift (Nascent Hispanic Corridor)
PANGAEA
60ºS
Karoo-Ferrar Province (183 Ma)
● OAE Organic-rich facies
○ CIE identified
b
90 Ma
HALIP
60ºN
LARAMIDIA
North America
WIS
Europe
Eurasia
PACIFIC OCEAN
ATLANTIC
TETHYS OCEAN
Shatsky
Hess
120ºW
60ºW
0º
60ºE
120ºE
0º
Mariana
Africa
South America
India
Ontong-Java Plateau
Australia
Uplift of South African Plateau
60ºS
Antarctica
Mountains
Landmass
Shallow sea
Deep ocean
Large igneous province
Mid-ocean ridge
● OAE organic-rich facies
○ Organic-lean sediments showing CIE
WIS Western Interior Seaway

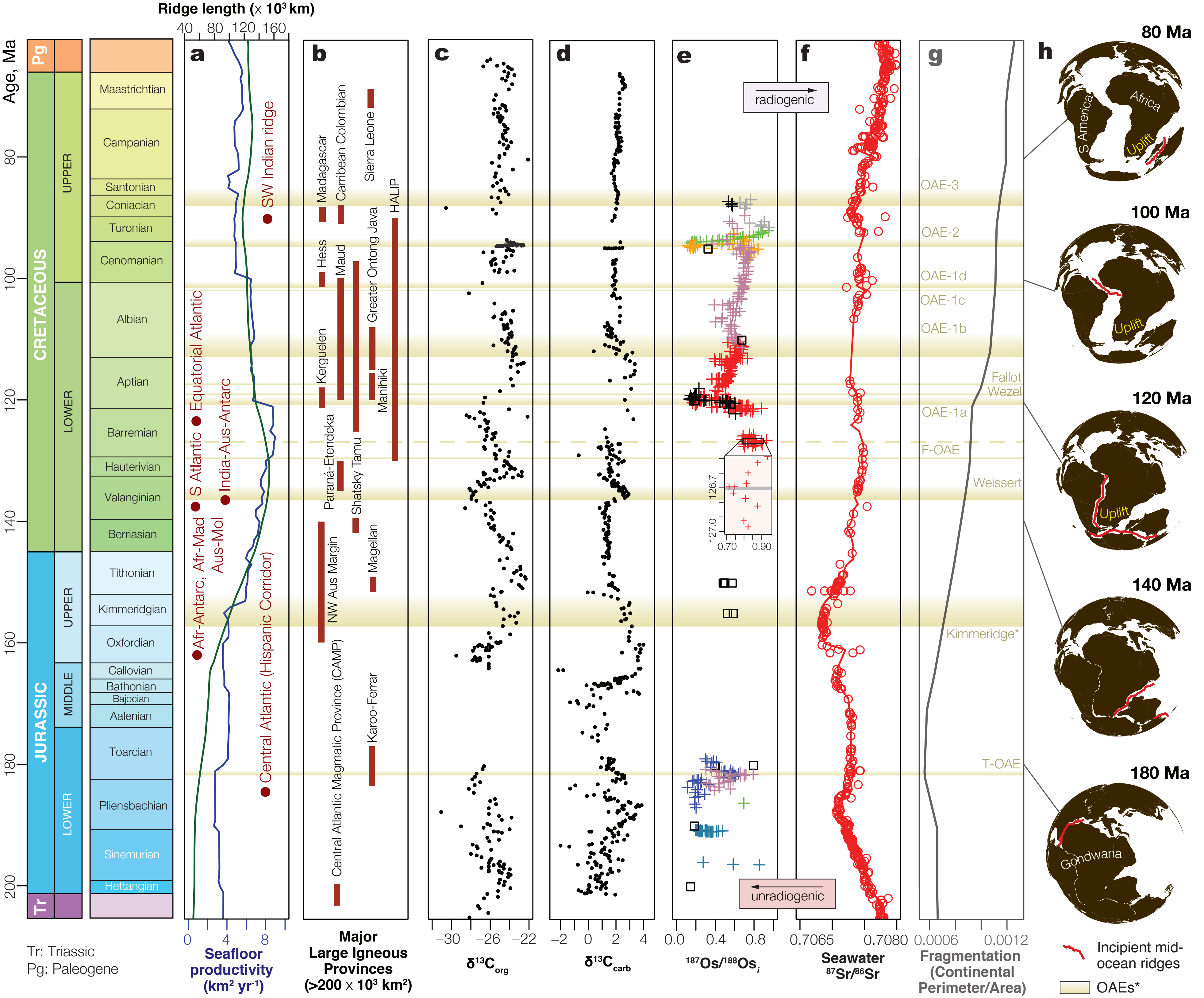
Age, Ma
80
100
120
140
160
180
200
Pg
CRETACEOUS
JURASSIC
Tr
UPPER
LOWER
UPPER
MIDDLE
LOWER
Maastrichtian
Campanian
Santonian
Coniacian
Turonian
Cenomanian
Albian
Aptian
Barremian
Hauterivian
Valanginian
Berriasian
Tithonian
Kimmeridgian
Oxfordian
Callovian
Bathonian
Bajocian
Aalenian
Toarcian
Pliensbachian
Sinemurian
Hettangian
Tr: Triassic
Pg: Paleogene
Ridge length (x 10³ km)
40 80 120 160
a
SW Indian ridge
Equatorial Atlantic
S Atlantic
India-Aus-Antarc
Afr-Antarc, Afr-Mad
Aus-Mol
Central Atlantic (Hispanic Corridor)
0 4 8
Seafloor productivity (km² yr⁻¹)
b
Madagascar
Caribbean Colombian
Sierra Leone
HALIP
Hess
Maud
Greater Ontong Java
Kerguelen
Manihiki
Paraná-Etendeka
Shatsky Tamu
NW Aus Margin
Magellan
Central Atlantic Magmatic Province (CAMP)
Karoo-Ferrar
Major Large Igneous Provinces (>200 x 10³ km²)
c
−30 −26 −22
δ¹³C_org
d
−2 0 2 4
δ¹³C_carb
e
radiogenic
unradiogenic
126.7
127.0
0.70 0.90
0.0 0.4 0.8
¹⁸⁷Os/¹⁸⁸Os_i
f
0.7065 0.7080
Seawater ⁸⁷Sr/⁸⁶Sr
g
OAE-3
OAE-2
OAE-1d
OAE-1c
OAE-1b
Fallot
Wezel
OAE-1a
F-OAE
Weissert
Kimmeridge*
T-OAE
0.0006 0.0012
Fragmentation (Continental Perimeter/Area)
h
80 Ma
S America
Africa
Uplift
100 Ma
Uplift
120 Ma
Uplift
140 Ma
180 Ma
Gondwana
Incipient mid-ocean ridges
OAEs*

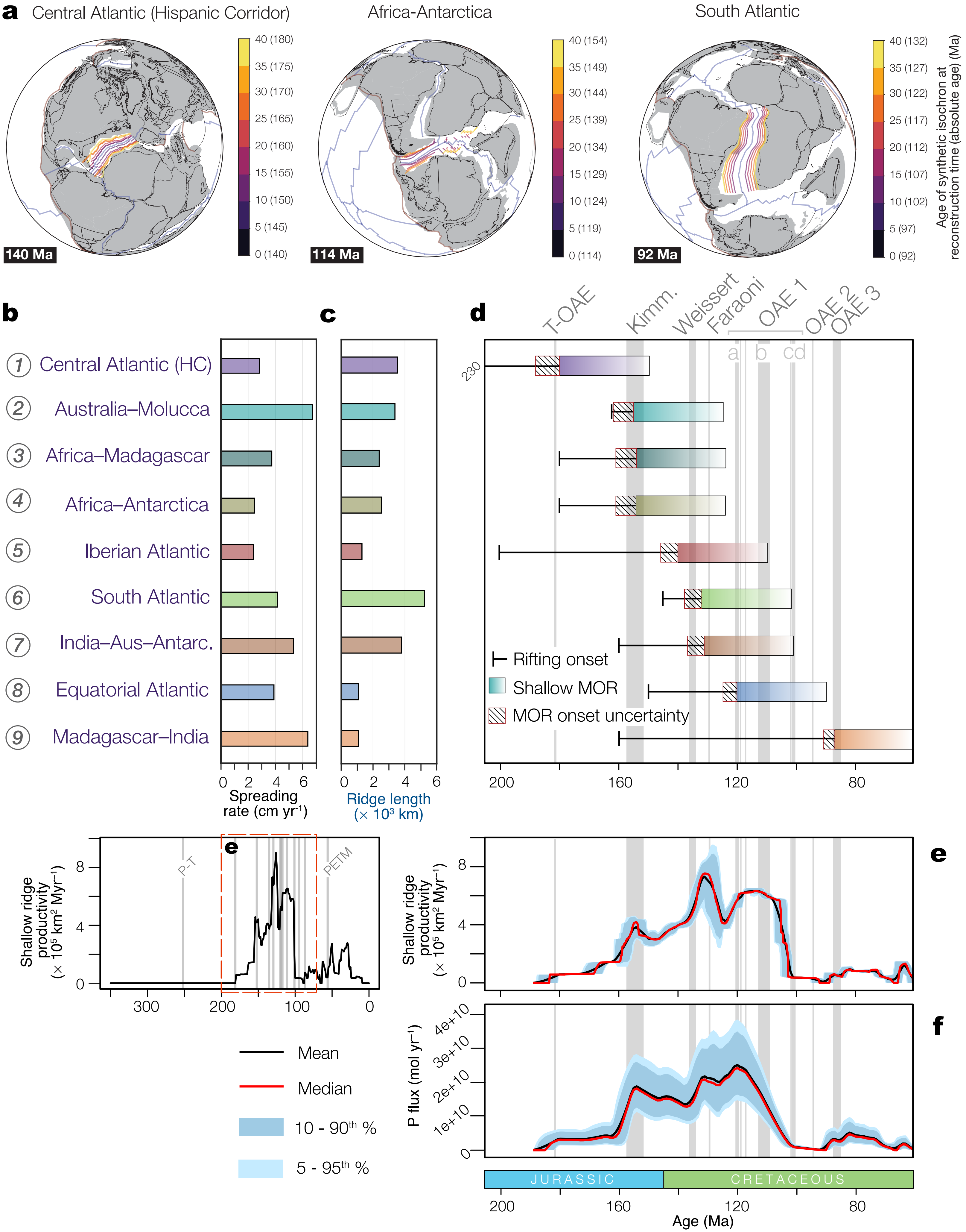
a
Central Atlantic (Hispanic Corridor)
Africa-Antarctica
South Atlantic
140 Ma
114 Ma
92 Ma
40 (180)
35 (175)
30 (170)
25 (165)
20 (160)
15 (155)
10 (150)
5 (145)
0 (140)
40 (154)
35 (149)
30 (144)
25 (139)
20 (134)
15 (129)
10 (124)
5 (119)
0 (114)
40 (132)
35 (127)
30 (122)
25 (117)
20 (112)
15 (107)
10 (102)
5 (97)
0 (92)
Age of synthetic isochron at reconstruction time (absolute age) (Ma)
b
c
d
① Central Atlantic (HC)
② Australia–Molucca
③ Africa–Madagascar
④ Africa–Antarctica
⑤ Iberian Atlantic
⑥ South Atlantic
⑦ India–Aus–Antarc.
⑧ Equatorial Atlantic
⑨ Madagascar–India
0 2 4 6
Spreading rate (cm yr⁻¹)
0 2 4 6
Ridge length (× 10³ km)
T-OAE
Kimm.
Weissert
Faraoni
OAE 1
OAE 2
OAE 3
a
b
cd
230
Rifting onset
Shallow MOR
MOR onset uncertainty
200
160
120
80
e
P-T
PETM
Shallow ridge productivity (× 10⁵ km² Myr⁻¹)
0
4
8
300
200
100
0
Mean
Median
10 - 90th %
5 - 95th %
e
f
P flux (mol yr⁻¹)
0
1e+10
2e+10
3e+10
4e+10
JURASSIC
CRETACEOUS
200
160
120
80
Age (Ma)

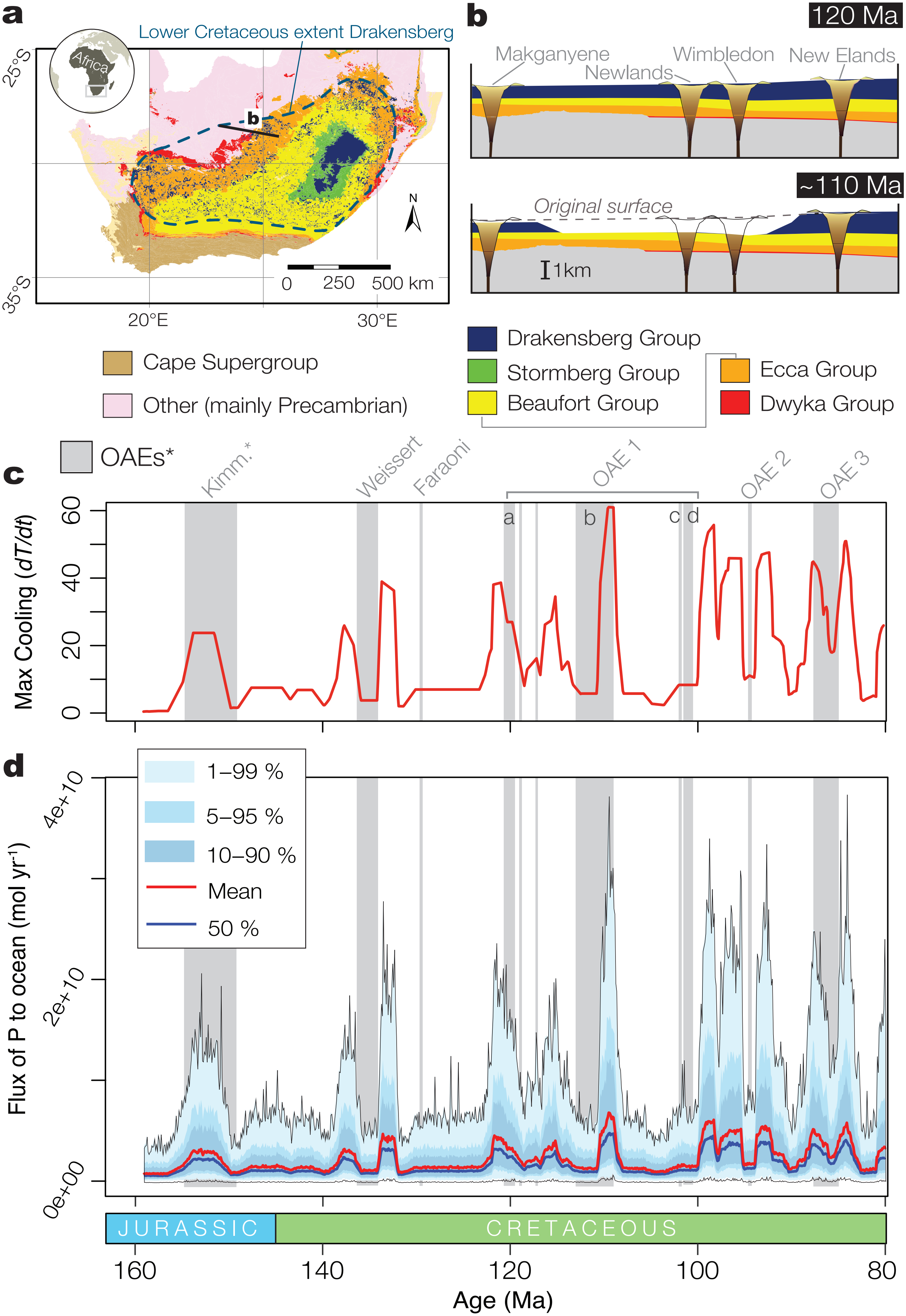
a
Lower Cretaceous extent Drakensberg
Africa
25°S
35°S
20°E
30°E
N
0
250
500 km
Cape Supergroup
Other (mainly Precambrian)
b
120 Ma
Makganyene
Newlands
Wimbledon
New Elands
~110 Ma
Original surface
1km
Drakensberg Group
Stormberg Group
Beaufort Group
Ecca Group
Dwyka Group
OAEs*
c
Kimm.*
Weissert
Faraoni
OAE 1
OAE 2
OAE 3
a
b
c
d
Max Cooling (dT/dt)
0
20
40
60
d
1–99 %
5–95 %
10–90 %
Mean
50 %
Flux of P to ocean (mol yr-1)
0e+00
2e+10
4e+10
JURASSIC
CRETACEOUS
160
140
120
100
80
Age (Ma)

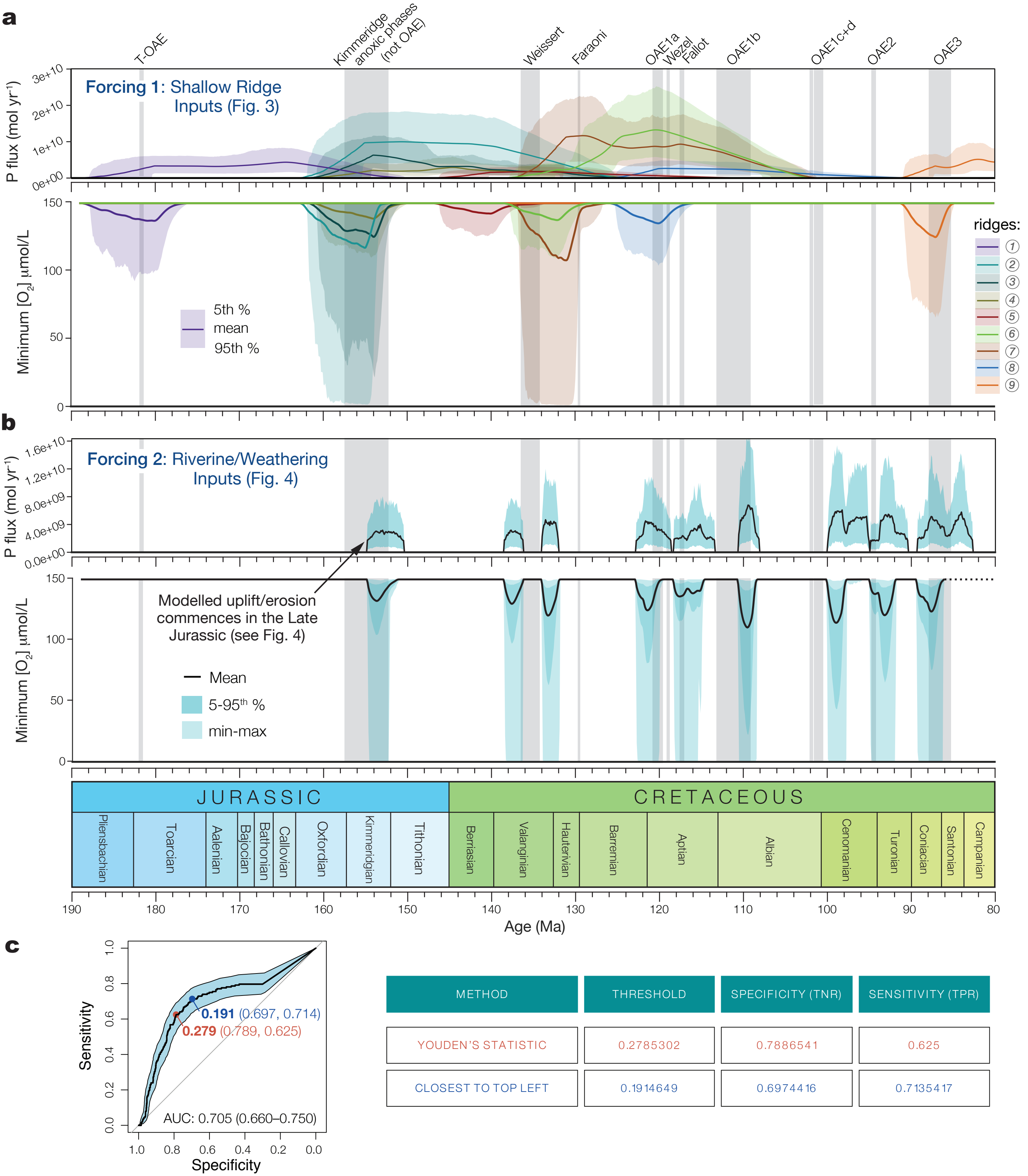

METHOD	THRESHOLD	SPECIFICITY (TNR)	SENSITIVITY (TPR)
YOUDEN'S STATISTIC	0.2785302	0.7886541	0.625
CLOSEST TO TOP LEFT	0.1914649	0.6974416	0.7135417